Integration and Testing of a High Temperature Superconductor Magnet with a Central Cathode Electrostatic Thruster

Chris R. Acheson[★†], *Jakub Glowacki*[★], *Ryota Nakano*[‡], *Daiki Maeshima*[‡], *Dominik Saile*[★], *Betina Pavri*[★], *Ryoyu Mori*[‡],
Ryohei Takagi[‡], *Randy Pollock*[★], *Jamal R. Olatunji*[★], *Max Goddard-Winchester*[★], *Nick Strickland*[★], *Daisuke Ichihara*[‡],
Stuart C. Wimbush[★] *and Kiyoshi Kinefuchi*[‡]
[★]*Robinson Research Institute, 69 Gracefield Road, Lower Hutt 5010, New Zealand*
[‡] *Department Aerospace Engineering, Nagoya University, Nagoya, Aichi 464-8603, Japan*
chris.acheson@vuw.ac.nz [†]Corresponding author

Abstract

Superconductor magnets generate high magnetic fields which can increase the performance of electric propulsion devices, but many such thruster operational regimes remain unexplored. In this work, a superconductor magnet and electrostatic thruster were integrated on a thrust measurement stand. Thruster performance was characterised at applied fields of up to 0.8 T, representing a significant advance for applied-field plasma thrusters. Thermal behaviour of the cryogenic magnet was assessed. A convex anode enabled ignition at high magnetic fields, and in this configuration thruster performance was measured in the range of 1 kW to 2.5 kW and 0.6 T to 0.8 T.

1. Introduction

Electrostatic ion acceleration devices such as Hall Effect Thrusters (HETs) and Gridded Ion Thrusters (GITs) have been demonstrated in space and allow a wide range of specific impulse values to be achieved.[1] This has enabled many ambitious missions, including Dawn[2] whose electric propulsion system operated for more than 50 000 hours during its multiple orbits of Vesta and Ceres, and the Hayabusa mission,[3] in which a spacecraft landed on Itokawa asteroid, mined it for samples, and returned those samples to Earth, prompting the Hayabusa2 successor mission to 162173 Ryugu. However, there are significant mission requirements on the horizon that these thrusters will not address in their current form. Thrust density of these electrostatic thrusters is fundamentally limited[1,4]— for example, NASA's NEXT GIT produces 2.3 N m^{-2} at 6.9 W,[5] and Busek's BHT8000 HET produces 9.1 N m^{-2} at 1.8 kW.[6] To access higher thruster output power and higher thrust operating points, the surface area of these thrusters must be increased. A significant aspiration for the electric propulsion community is therefore to design a thruster with a higher thrust density limit which could be throttled across a wider range of thrusts and output powers without requiring a larger surface area. One envisioned future for such a high thrust density device is on an interplanetary cargo ship, utilising a small mass of propellant to slowly move a large payload mass to a distant destination. Applied Field Magnetoplasmadynamic Thrusters (AF-MPDTs) are a promising candidate, and have been operated at thrust densities of more than 10 kN m^{-2} for a very high input power of 2.8 MW.[4,7] AF-MPDTs rely on an electromagnetic acceleration mechanism (with supplementary electrothermal acceleration) to accelerate plasma propellant along the thrust axis.[8] Coupling the high thrust density of an AF-MPDT with the high performance of electrostatic thrusters is desirable, and this provides the motivation for the development of the Central-Cathode Electrostatic Thruster (CC-EST).[9] This thruster has a similar design to a gas-fed AF-MPDT, but an insulator block between cathode and anode is used to create an electrostatic potential drop which accelerates propellant ions which are injected close to the anode. These thrusters have been demonstrated to produce thrust densities of up to 70 N m^{-2}.[10] One notable aspect of this CC-EST layout is that, unlike for HETs, strong magnetic fields can be used without inhibiting the mechanism of electrostatic thruster operation. Measuring CC-EST performance at different magnetic fields is consequently a topic of considerable interest. Furthermore, operating the CC-EST at the kW power level (which is achievable on a small satellite) is a target which could have near-term real-world applications, and there are two key scientific questions for the CC-EST in such a regime. Firstly, there are fundamental limits on low power operation in that the thruster will not ignite below a certain discharge voltage. Minimum discharge voltage depends on other operating conditions, such as mass flow rate and applied field.[11] Finding those limits is key to gaining an understanding of the underlying physics. Secondly,

INTEGRATION AND TESTING OF A SUPERCONDUCTOR MAGNET WITH A PLASMA THRUSTER

Parameter	CC-EST		AF-MPDT			
	this work	Sasoh et al.[13]	Ichihara et al.[14]	Voronov et al.[15]	Tahara et al.[16]	Zheng et al.[17]
J_d (A)	2.7–7.8	–	10–20	450–600	1200–2900	700
B (mT)	300–800	100–250	133–265	0–750	45–90	200–560
$\dot{m}$ (mg/s)	1.9–5.5	1.17–2.54	0.83–3.9	10–50	45–126	40–70
P_d+P_k (kW)	0.71–2.39	–	0.76–3.26	5.5–27.5	–	150

Table 1: Thruster test parameters for this work compared to previous publications for CC-ESTs and AF-MPDTs, where J_d is anode discharge current, B is applied magnetic field at the centre of the bore, $\dot{m}$ is the propellant mass flow rate, and P_d and P_k are the anode discharge power and the keeper discharge power respectively.

previous work on low power AF-MPDT operation has indicated that efficiency increases with magnetic field.[12] It is therefore interesting to investigate whether the CC-EST follows the same pattern. CC-EST performance in the kW range has been characterised at magnetic fields of up to 250 mT,[9] with limits on the magnetic field imposed by the copper electromagnet. A HTS magnet would allow the thruster to be tested at higher magnetic fields. A HTS magnet has not previously been integrated with a CC-EST. However, there have recently been two experimental studies of HTS AF-MPDTs.[15, 17] These both investigated high power, high current AF-MPDT operation, with discharge currents in the 100s of A range. Operating conditions for these thrusters are shown in Table 1, which are shown alongside previous CC-EST and AF-MPDT study data. In addition to experimental campaigns, there have been theoretical and commercial studies on the topic of HTS magnets for plasma thruster applied field modules.[8, 18, 19]

A superconductor magnet therefore enables investigation of a CC-EST's performance in the high field, low power regime. High temperature superconductor (HTS) materials can be used to create high field magnets,[20] and have long been perceived as futuristic solutions to many problems in space. Potential uses include magnetic shielding from cosmic rays,[21] energy storage and power conditioning,[22] and propulsion applications.[8] These materials have zero electrical resistivity at temperatures below their critical temperature. For practical applications, 77 K is often considered a maximum useful operating temperature in a HTS magnet. The HTS material will remain in the superconducting state provided the current in the HTS remains below the critical current. Critical current decreases with increasing magnetic field and increasing temperature. The use of superconducting wire in an applied field module comes with the penalty of the necessary subsystems. For continuous operation, this includes a power supply and a cryocooler (with its own power supply, control system and thermal management subsystem). Superconducting wire is also expensive and mechanically fragile compared to copper. Its inclusion must therefore be justified by superior performance. There have been several barriers to adopting this technology, such as cost and engineering complexity. There has also been a persisting perception that cryogenic fluids such as liquid nitrogen or supercritical helium are required to provide sufficient cooling to the HTS materials. The two previous examples of HTS plasma thrusters used cryogenic fluid[15, 17] to cool the magnet. This has the advantage of providing a very high cooling power directly to the magnet, but a convective cryogenic fluid cooling system for space applications would have a number of disadvantages (including sloshing, leakage, complexity, and mass) compared to a solid, conductive magnet cooling system.

With this in mind, we built a HTS magnet system in which many of the problems involved with space deployment were solved. The operating requirements were limited to the following: power for the magnet supplied by two power wires which require input power on the level of 1 W to 10s of W; power for the cryogenic thermal management system using a further two wires with a power requirement of less than 100 W; no cryogenic fluid other than the internal working fluid of a sealed commercial off-the-shelf (COTS) version of a space qualified cryocooler; and 10 °C cooling requirements on the order of 100 W. This magnet represents a significant step towards a spaceflight capable HTS magnet.

The HTS magnet was used as the applied field module for a CC-EST. The performance of the thruster was measured in a low power, high magnetic field regime— the first measurements of a CC-EST, or indeed any applied-field plasma thruster, in this regime.

2. Methods

A plasma thruster was assembled with a superconductor magnet and cryocooler, and suspended on a hanging pendulum thrust stand. The thruster's performance was characterised under a range of different operating conditions, which can be found in Table 1. An operational parameter search was performed to find a set of appropriate operating conditions which would allow reliable plasma thruster ignition at the high magnetic fields which could be created using the HTS

magnet.

2.1 HTS CC-EST assembly

The CC-EST and HTS magnet assembly is shown in Fig. 1. a) shows the assembly with cryocooler and magnet around the thruster. The magnet bore radius is 50mm. Between the outer anode wall and the HTS coils, there was an alumina annulus and bobbin-shaped stainless steel magnet housing. The magnet was vacuum suspended from the stainless steel magnet housing using G10 plates to lengthen the conductive pathway to the magnet, and two layers of MLI (10 sheets per layer) were wrapped around the cryogenic section. Details of the thermal design of the HTS magnet can be found in a dedicated publication.[23]

The magnet was powered using a CAENels FAST-PS-1K5. The magnet power supply output current J_m and voltage V_m were measured. This allowed the power output of the magnet power supply to be calculated. The current leads were thermally anchored to a water cooling system on the thrust stand. This ensured that the temperature of the current leads close to the magnet was held constant at 10 °C, and thus prevented Joule heating from the full length of the current leads conducting into the magnet. The power utilised by the water chiller was not recorded. The magnet was conductively cooled using a cryocooler (Cryotel MT, Sunpower Inc.), and the power output of the cryocooler controller was recorded. The cryocooler cold head was rigidly mounted to a copper thermal bus as shown in Fig. 1 a). This thermal bus was anchored to copper sandwich plates between coils and thus provided a thermally conductive cooling path to each of the magnet coils. Fig. 1 a) shows the location of the temperature sensor which was used to monitor the magnet temperature. Note that, with the cryocooler on, the temperature here will be lower than at other locations within the magnet because heat is extracted at the cryocooler cold head. By using conductive cooling, there was no cryogen used in the HTS cooling system, with the exception of the internal working fluid of the 2.1 kg COTS cryocooler.

A closeup of the CC-EST with a cylindrical anode is shown in Fig. 1 b). The cathode is a hollow heaterless cathode, which was operated continuously during the experiments with a mass flow rate (termed the cathode mass flow rate) of 0.5mg/s Xe. Close to the anode, there is a slit in the insulator through which propellant mass is introduced. This anode slit is present in Fig. 1 b) and c), with the position indicated in c). The mass flow rate here (termed the anode mass flow rate) varied between 1.3mg/s and 5.0mg/s, and was either Xe only or a mixture of Ar+Xe. Fig. 1 c) shows the CC-EST with an additional anode ring, which created a convex anode.[24] This expanded the operating range of the thruster at high fields.

2.2 Plasma plume analysis

Plasma characterisation is useful for deriving underlying physical phenomena behind thrust generation in electric thrusters. Many intrusive diagnostic tools exist, such as Langmuir probes, Faraday cups, and Retarding Potential Analysers. However, these diagnostic tools disturb the plasma plume and therefore do not give a true measurement of an unperturbed plume. Optical measurements in the form of plasma plume videos are an alternative plume diagnostic tool which can be set up without any a priori knowledge of the plasma, and without interfering with the plasma itself. Other research groups have used optical measurements to predict plasma parameters such as the electron temperature and number density.[25] Optical measurements are also useful in classifying the plasma plume structure.[26] During our experiments, videos were taken of the thruster during operation, with the camera at the position shown in Fig. 1 a). These videos were used to analyse the plume according to the method outlined below. The same videos were further utilised for debugging when the thruster system's behaviour was not as expected. For instance, there were several abnormal discharges: that is, occasions where the anode discharged to something other than the cathode. By observing the video footage, the precise locations of these discharges could be identified for repair.

Video recordings were made with a Sony IMX555 CMOS image sensor which facilitates video recording with a spatial resolution of 1080 px by 1920 px at a recording frequency of 30 Hz. The incoming light is filtered on the chip into a red, green and blue channel. The exact spectral sensitivity function is not known. It is assumed that the blue, green, and red channel capture light in the ranges of 400 nm and 550 nm, 450 nm and 630 nm, 560 nm and 700 - 1000 nm, respectively.

In post-processing, the thruster exit along the center line was identified by visual inspection and defined as the origin. The image was tilt-corrected and scaled, and then features of interest were identified and their size and shape were measured.
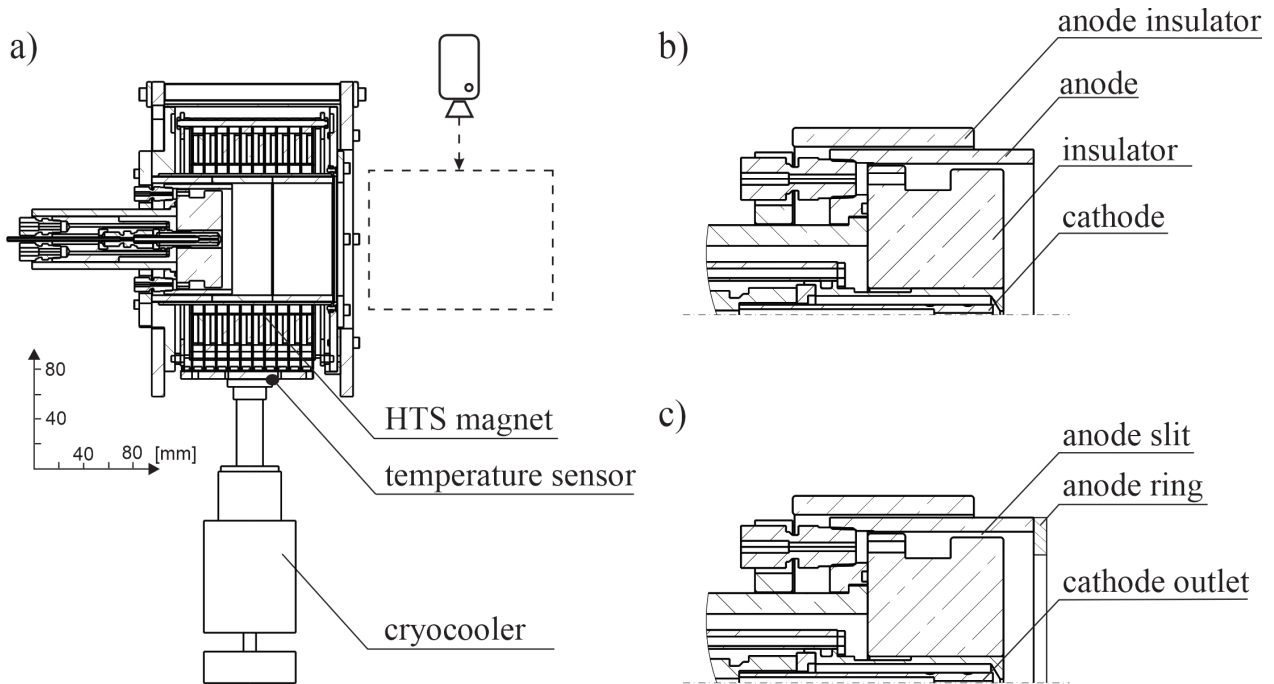
Figure 1: Diagram of the CC-EST and HTS magnet assembly used in testing. This assembly was mounted on a suspended thrust stand internal to a vacuum chamber (not shown). a) The CC-EST was mounted in bore of the HTS magnet. The HTS magnet temperature was maintained by a cryocooler mounted to a copper "thermal bus" which was conductively coupled to the magnet coils. A camera external to the vacuum chamber captured visual data showing the effect of the HTS magnetic field on the plasma during testing. b) close-up of "cylinder" thruster configuration. c) close-up of "convex" thruster configuration, where an anode ring is used to reduce the inner diameter of the anode.

2.3 Thruster performance analysis

The thruster was mounted on a hanging pendulum thrust stand with an arm length of 1 m. A bellows-bearing pivot point allowed the pendulum to oscillate and provided the vacuum seal. The angular position of the thrust stand was measured using an externally mounted Linear Variable Differential Transformer (LVDT) (LVDT1301-2, Shinko Electric Co., Ltd.). The thrust stand's position as a function of applied force was calibrated using a motor actuated mass-on-string pulley system. Propellant was supplied to the thruster using three Mass Flow Controllers (MFCs) (3660 series, Kofloc, Inc.), with two MFCs supplying the anode with gas and one MFC supplying the cathode with 0.5 mg/s Xenon. This enabled the use of an anode gas mixture of Argon and Xenon, or operation using only Xenon. The tantalum hollow cathode was powered using a Kaufman & Robinson KC8002 keeper controller with a constant discharge current of 2 A. The anode was powered using a DC power supply (HX01000-12M2I, Takasago Ltd.). A NI-DAQ data acquisition system was used to measure the keeper voltage, anode voltage and anode current. Limits on thrust were imposed by the maximum discharge voltage of 400 V (chosen to protect equipment from abnormal discharge), and the maximum mass flow rate of the MFCs of 5.5 mg/s — as such, the measurements are a reflection on the upper power limits of the measurement system, not the upper limits of the thruster. However, the lower power limits presented here are intrinsic to the thruster.

It was important to characterise the interaction of the thruster and thrust stand with the magnet and cryocooler. Lorentz force interactions between the discharge current and the magnet were found to account for up to 2.4 mN of the measured thrust but were not measured for every case, so this value was considered as a source of error. In addition, the mechanical interaction between the vibrating cryocooler and the hanging pendulum thrust stand was investigated by firing the thruster with the cryocooler either on or off, and investigating the differences in the LVDT signal to noise in each case. The results of this investigation are shown in subsection 3.1.

Using these measurements, the performance of the thruster was characterised using the following equations. Specific impulse was estimated from the thrust and the mass flow rate:

$$I_{sp} = \frac{F_T}{\dot{m}g} \tag{1}$$

where I_{sp} is specific impulse, F_T is thrust force, $\dot{m}$ is propellant mass flow rate (which is inclusive of cathode and anode

mass flow rate, unless stated otherwise), g is the gravitational constant. The efficiency of the thruster was calculated using:

$$\eta = \frac{F_T^2}{2\dot{m}P} \tag{2}$$

where η is efficiency, and P is total power. Equations 1 and 2 can be combined to show the relationship between specific impulse and thrust per power:

$$\frac{F_T}{P} = \frac{2\eta}{I_{sp}g} \tag{3}$$

Total power can be expressed as the sum of contributions:

$$P = P_d + P_k + P_m + P_{cc} = V_d J_d + V_k J_k + V_m J_m + P_{cc} \tag{4}$$

where P_d is the anode discharge power, P_k is the keeper discharge power, P_m is the power output by the magnet power supply, P_{cc} is the power output by the cryocooler power supply, V is voltage, J is current, and the subscripts for V and J are the same as those for P. Water cooling was provided to capture the cryocooler's rejected heat in the vacuum chamber, in lieu of passive radiative cooling that would traditionally be used in space applications. One of the standout points of this study is that the power utilisation of the cryocooler and magnet system is included in the power and efficiency reporting. This has not been reported in studies using cryogenic fluid cooling loops.[15, 17]

3. Results and discussion

3.1 Cryocooler and magnet operation

Fig. 2 shows the LVDT voltage (which is negatively proportional to thrust) as a function of time. Initially, thrust measurements were taken with the cryocooler on. During operation, the cryocooler piston operates at 60 Hz. There was some energy coupling between the cryocooler and the thrust stand natural pendulum frequency. Therefore, in taking a measurement with the cryocooler on, not only was the signal to noise ratio lower, but the signal itself was also impacted. Thrust measurements made with the cryocooler on thus had larger errors. To extract a thrust signal, the "cryocooler on" data were smoothed using a moving average with window equal to the period of oscillation of the hanging pendulum thrust stand. The mean of this moving average was compared between thruster on and thruster off, and the voltage difference was converted to a force using a previously determined calibration curve of LVDT response to application of known force. In cases where the measured force was greater than the calibration weight, extrapolation was used, which was a source of error. In later experiments (i.e. those with the convex anode), the calibration weight was increased to ensure that force measurements fell within the calibration range. With the cryocooler off, LVDT noise was significantly reduced. For fair comparison, the same moving average method was also used to process the thrust data when the cryocooler was off. Fig. 2 demonstrates that the thrust stand oscillates less when the cryocooler is off, and the signal is therefore less noisy. The signal is also not impacted by energy coupling between cryocooler vibration and thrust stand oscillation when measurements are made with the cryocooler off. For this reason, measurements were made with the cryocooler off when possible.

Turning off the cryocooler to gather thrust data had a significant influence on the magnet temperature. The temperature is shown as a function of time in Fig. 3. This temperature is measured at the connection point of the cryocooler cold tip to the magnet thermal bus (as shown in Fig. 1 a)), and therefore this is the position of the magnet which is coldest when the cryocooler is on, and which will have the greatest dT/dt when the operational state of the cryocooler is changed. To take thrust measurements, two different procedures are shown in Fig. 3b. Around the 700s mark, a measurement is taken by the following procedure. The magnet was at steady state, having had a constant current in the coils for a period of time much greater than the charging time of the magnet. The hollow cathode was running with a mass flow rate of 0.5 mg/s and constant discharge current of 2 A. To initiate the measurement procedure, the cryocooler was turned off, causing the magnet temperature to begin to rise. The gas flow at the anode was initiated concurrently. Once the vacuum chamber back pressure had levelled off and the cryocooler vibrations could no longer be seen in the LVDT voltage, the thruster was ignited by applying a discharge voltage to the anode. Thruster discharge was sustained for 5 to 20 seconds. The discharge was then stopped by setting the discharge voltage to zero, and after a few seconds the anode gas flow was ceased and the cryocooler was turned on again. The process was repeated with the cryocooler on at 950 s. The hollow cathode and magnet remained in the same operational states through the whole procedure, and during the period between thruster discharges. From Fig. 3b, it is clear that turning the cryocooler off and igniting the thruster had a much larger impact on the magnet temperature than igniting the thruster alone.
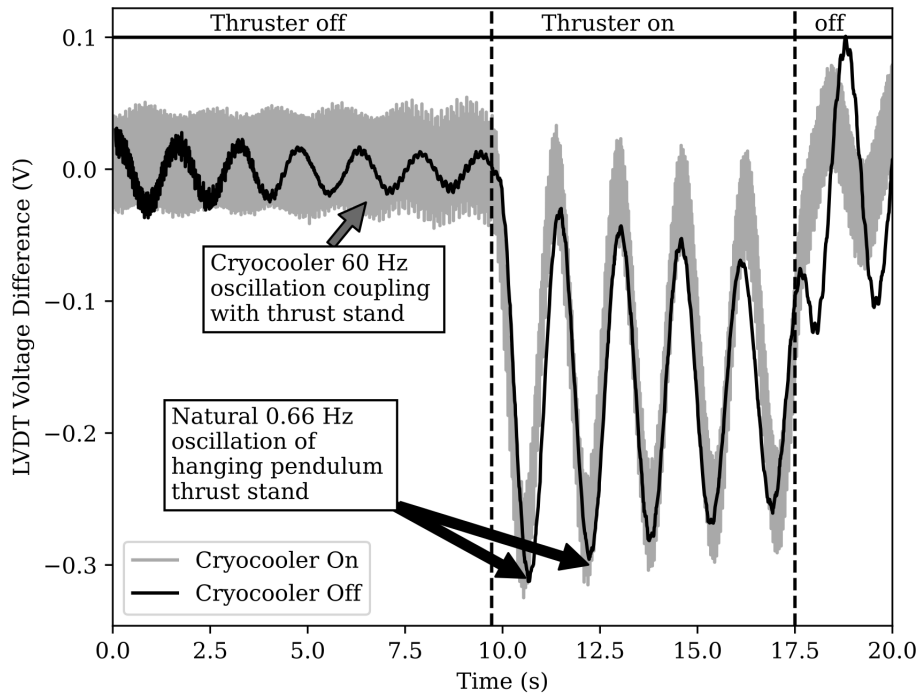
Figure 2: Thrust vs time for example cases with the cryocooler on and off. The cryocooler caused vibration through the thrust stand which impacted the clarity of the LVDT signal.

Fig. 3a shows that the temperature of the magnet rises significantly each time the cryocooler is switched off to take a measurement. This means that there is a finite number of measurements that can be taken in quick succession before the magnet will exceed its safe operating temperature. The higher the magnetic field, the higher the magnet current and therefore the larger the heat load on the magnet from heat leak via the copper connection leads (in which Joule heating occurs). The temperature trend is therefore steeper for higher magnetic fields, and so fewer measurements can be taken at high field before the magnet exceeds critical temperature. Furthermore, the higher the magnetic field, the lower the critical current, and therefore the lower the safe operating temperature of the magnet. Thus at high fields, the temperature limit is lower and it is approached faster.

The HTS magnet was operated at a range of different fields, and the power output by the magnet power supply, P_m, was measured. The magnetic field was calculated using a current calibration curve and was not measured directly during thruster experiments. Each double-pancake coil had a voltage tap pair which could be used to measure the voltage drop across the HTS tape in the magnet. At 28.6 A (producing an on-axis bore field of 1.1 T), less than 4 mV per coil was achieved, corresponding to less than 1 W of heat loss in the HTS tape. However, P_m=45 W in this case, demonstrating that the resistive parts of the magnet circuit were the main locations of heating, not the HTS magnet coils. At 0.8 T, P_m=22 W and at 0.5 T, P_m=9 W. Therefore, the power lost in the magnet was a fraction of the total power output of the magnet power supply, with most of the power loss occurring in the current leads and electrical connections between the magnet power supply and the magnet rather than in the magnet itself.

3.2 Integration of magnet instrumentation with thruster and thrust stand

One of the challenges of integrating the magnet with the thruster and thrust stand was taking precise and accurate measurements of many different physical parameters without the different measurement systems interfering with one another. HTS magnets are high performance devices, provided they are kept within acceptable operating conditions. The magnet coils used in this study were no-insulation coils[27] and are therefore robust to quench to an extent. However, it is still possible to damage a magnet if key locations in the superconductor tape quench, or if quench occurs throughout a large volume of superconductor.[28] It is therefore prudent to continuously monitor the status of the magnet in order to detect indications of imminent quench in the superconductor tape, and to de-energise the magnet before magnet failure
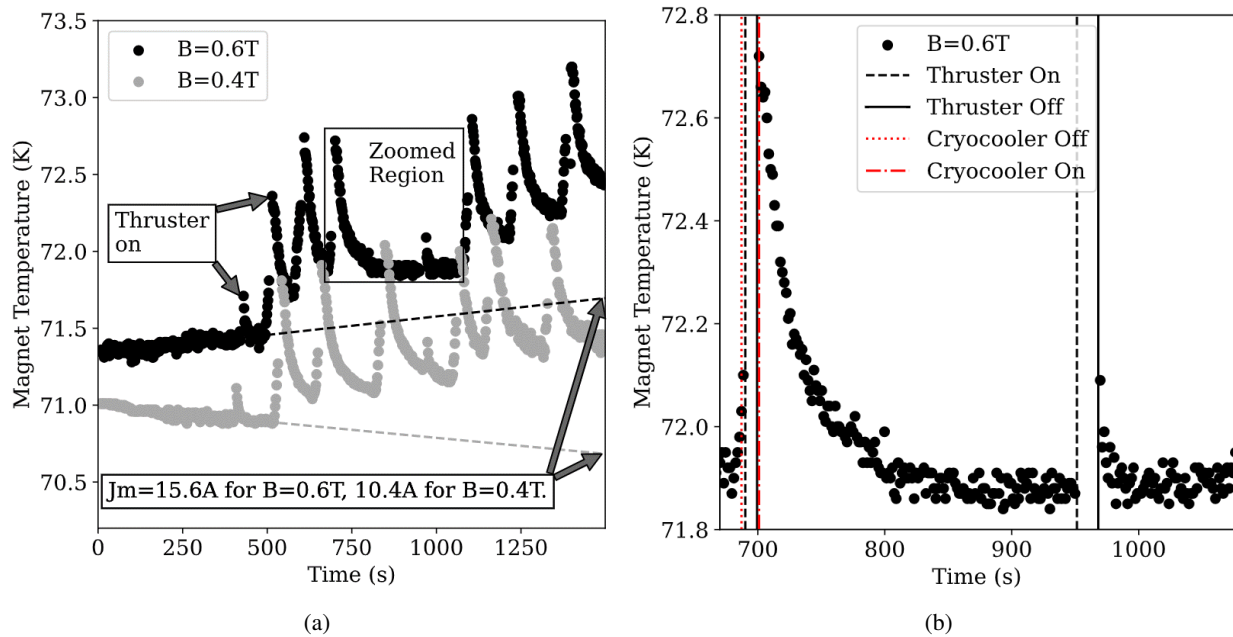
(a)　　　　　　　　　　　　　　(b)

Figure 3: Superconductor magnet temperature measured at the tip of the cryocooler plotted against time for a duration including multiple thruster discharges. a) Temperature plots of the superconductor magnet operating at 0.4T and 0.6T. Magnet current, J_m, is indicated for each field. Temperature trends (if the cryocooler were always on and the thruster were not discharged) are indicated by dashed lines for each magnetic fields. Higher magnetic fields result in higher magnet equilibrium temperature and greater (i.e. more positive) rate of temperature change. However, the greatest change in temperature is the result of turning the cryocooler off. While the thruster was operating, there was too much noise in the temperature sensor wires to take a measurement. b) Zoomed-in 0.6T magnet operation. This shows the standard procedure for thrust data collection of both methods— cryocooler on and cryocooler off.

occurs. To monitor the magnet status, numerous sensors (and the wiring to read them) were installed. Each magnet coil "double pancake" set had a corresponding pair of voltage taps and pair of wires for a temperature sensor. There were also many additional temperature sensors mounted to the exterior of the magnet. In total, this required more than 50 magnet sensor wires. During one thruster discharge, an exposed electrical connector for a temperature sensor was subject to an abnormal discharge from the anode, which resulted in the failure of the temperature monitor. To prevent damage to further equipment, mylar sheets and Kapton tape were used to insulate the instrumentation electrical connections. This added rigidity and mass to the instrumentation wires, altering the response of the thrust stand to an applied force. A change in pendulum spring constant is acceptable, but non-restorative forces such as friction reduce the accuracy of thrust measurements. Friction could occur between: rubbing wires; a wire and Mylar insulation; wires and the apparatus on the thrust stand; wires and equipment affixed to the chamber. Identification and elimination of friction sources is critical in order to take accurate and precise thrust measurements. In the "cylinder" anode configuration, the data presented here were gathered in a configuration with friction between wires, and hence the thrust measurements have larger errorbars than the "convex" anode configuration thrust data which were gathered after friction within the system had been eliminated.

3.3 Plasma plume analysis

Fig. 4 a) shows a representative picture of the thruster and the plume under operating conditions. The plume is clearly visible and three distinct regions can be identified: the bright center line from the thruster, the comparatively faint cone surrounding it, and finally a colorful region curving from the bore of the magnet toward the top and bottom of the chamber. The illumination along the center line is overexposed, meaning no characteristic features can be extracted from that region. The same is true for the cone-like structure since it does not exhibit clear distinguishing features. However, the curved portion of the plume can be analyzed to extract a maximum for comparisons between various thruster discharges. The local intensities are integrated along the line-of-sight, so the location of the maximum intensity does not necessarily align with the location of the physical maximum intensity.

To extract this characteristic maximum, the picture is scanned line by line for the maximum grey-value in the

INTEGRATION AND TESTING OF A SUPERCONDUCTOR MAGNET WITH A PLASMA THRUSTER
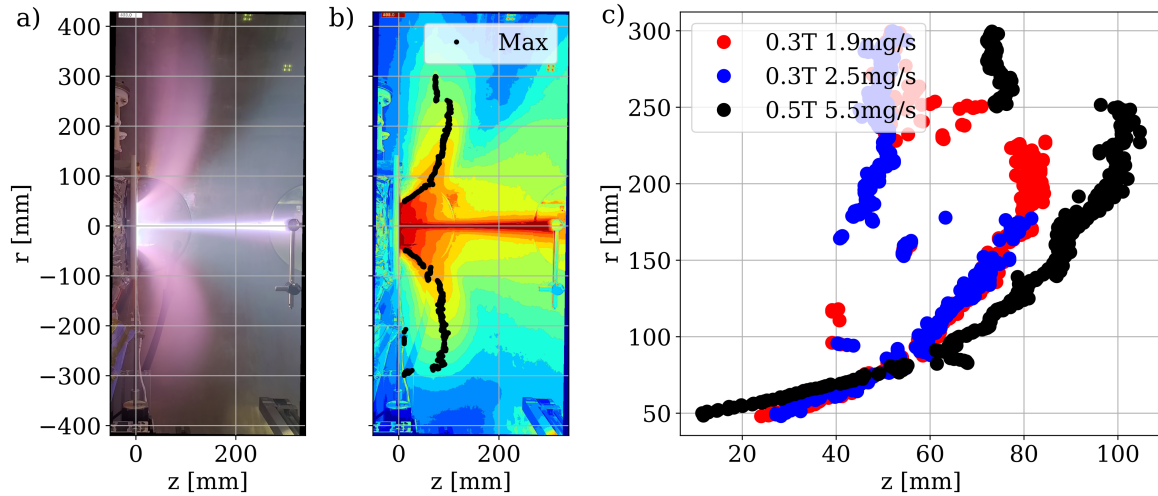

Figure 4: Video-still analysis of thruster plume. a) HTS CC-EST firing at 0.5 T, 250 V with 5.5 mg/s Xe-Ar mixture. Thruster is axisymmetric, with axial z direction and radial r direction shown. b) Contours of image intensity, with scatter plot of maximum intensity. c) Maximum intensity plots for thruster firing at 250V and different magnetic fields and mass flow rates. The propellant was Xe, with the exception of 0.5 T 5.5 mg/s, which was a Xe-Ar mixture.

vertical direction in the curved region of the plume. Due to the low dynamic range, the maximum intensity value occasionally latches onto the same value for an extended range. For this reason, the median of the consecutive maxima along a pixel line is defined as location for the maxima.

Fig. 4 b) shows the light intensity contour plot for the same image, and a representative result for this feature extraction approach. The maximum intensity line shown in black demonstrates that there is significant curvature in the plume. This indicates that there are charged particles which are tied to the magnetic field lines. This agrees with the findings of Han et al.,[25] which further showed that the particles tied to the field lines are highly magnetised electrons. Light is produced by the electron interaction with background neutrals. An intensity analysis for different plumes is shown in Fig. 4 c). The red and blue lines are overlaid up to r=150 mm, whereas the black line extends 11mm further in the z direction at r=150 mm. The difference in operating conditions between the red and blue lines is the mass flow rate, and therefore changing the mass flow rate does not have a large impact the shape of the plume at values of r less than 150 mm. At higher values of r, the algorithm picks out a feature at a lower z position for the blue (higher mass flow rate) line in the region from approx. r=175 mm. For the red (lower mass flow rate) line, a similar feature is also identified, but not until r=230 mm. Curvature is still observed. Differences between the black line and the red/blue lines are more pronounced through the whole region. The differences show that there is a significant response to the new operating conditions: namely, the increased magnetic field and the addition of supplementary Ar propellant. Having established that increasing the mass flow rate had a minimal impact on the plume shape, we can infer that this difference is caused by changing the magnetic field. An explanation for this behavior is provided by the theory of the magnetic nozzle[29] which proposes that currents in the plasma create a magnetic field which opposes the applied magnetic field, thus acting upon the thruster magnet and transferring force to the thruster.

3.4 Thruster performance

Thruster performance is shown in Fig. 5. On the left, Fig. 5 a), c) and e) show the performance of the thruster with the cylindrical anode. This is the same anode configuration used in previous studies.[13] The anode discharge voltage is annotated in e).The thruster was successfully ignited at 0.3 T using Xe as the only propellant, but not at 0.5 T. A mixture of Ar and Xe was used at 0.5 T. Fig. 5 a) shows thrust ranging from 26 mN to 82 mN with the highest thrust at 0.5 T corresponding to a specific impulse of 1540 s. This represents reasonably high performance, but thruster ignition was unreliable: only achieved in approximately half of the attempts. Ignition at 0.6 T with the cylindrical anode was attempted, but no stable discharges were achieved at discharge voltages of up to 400 V. It was therefore concluded that investigation of the thruster's performance at higher magnetic fields was not possible using the cylindrical anode configuration. The specific impulse is shown in Fig. 5 c). Specific impulse at 0.3 T using only Xe was recorded at more than 1600 s. As shown in Fig. 5 e), this was achieved at low power. By increasing the field and adding
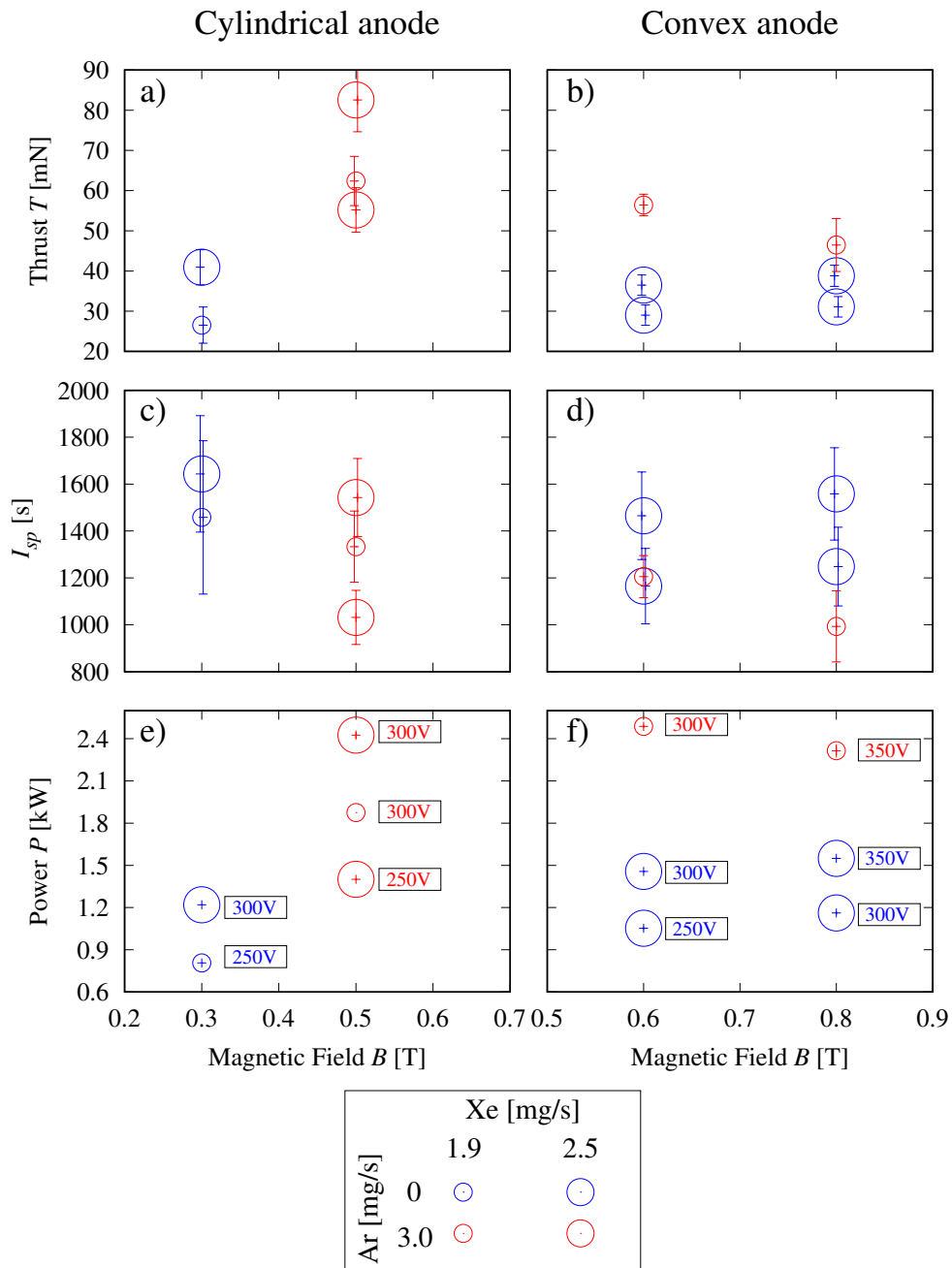
Figure 5: Performance of the HTS CC-EST in high magnetic field regime, with anode mass flow rates shown in the legend. Specific impulse values are inclusive of cathode and anode mass flow rates. Power represents total system power as described in Eq. 4.

supplementary Ar propellant at the anode, the power requirements increased and the specific impulse decreased. The power requirements increased due to the higher ionisation energy of Ar compared to Xe. At fields of both 0.3 T and 0.5 T, the thruster could operate at a range of powers, specific impulses and thrusts. Having discovered that thruster ignition at higher magnetic fields was not possible with this configuration, the thruster was modified with a convex anode as shown in Fig. 1 c).

The convex anode results are shown in Fig. 5 b), d) and f) for magnetic fields of 0.6 T and 0.8 T, and for the discharge voltages shown in f). The convex anode configuration enabled thruster ignition at higher magnetic fields, both with and without Ar propellant in addition to the Xe propellant. For example, at 0.6T the minimum discharge voltage was reduced from 400 V (with the cylindrical anode) to 250 V (with the convex anode). The thrust is shown in Fig. 5 b). The discharge voltage required for minimum power ignition increased with magnetic field. When Xe

was used as the propellant, the thrust measured at minimum power increased slightly with magnetic field. However, when Ar was used to supplement the flow of Xe the thrust was found to decrease with increasing magnetic field. Fig. 5 d) and f) also show decreases in Ar+Xe specific impulse and power with increasing magnetic field— contrary to the trends visible in the Xe only data. Investigation into the underlying cause revealed that the discharge current became unsteady during some Ar+Xe discharges at 0.8 T, with current dropouts causing a reduction in thruster power. This resulted in a loss of thrust and specific impulse. It should be noted that in general, the occurrence of discharge current oscillation does not necessitate a decrease in thruster performance, which may improve if the current oscillations enable sufficient power savings in the lower power operation mode. However, in this specific case the reduction in performance represented by this datapoint reflects the increasingly unsteady thruster discharge at higher magnetic fields. While this phenomenon has been reported in other HTS applied-field plasma thruster studies,[15,17] the discharge currents utilised in our experiments were much lower and the oscillation mechanism is probably different. In the Xe only operation no unsteady discharge current was observed, and the thrust and specific impulse at minimum discharge power increased with increasing magnetic field. The minimum discharge power also increased with increasing magnetic field. However, at a fixed discharge voltage and mass flow rate, the discharge power decreased with increasing magnetic field, indicating an increased resistivity of the plasma at higher magnetic field.

The performance of the thruster with convex anode is shown in Fig. 6, here with a) power, and b) thrust per power plotted against specific impulse. a) demonstrates that the power requirements with Ar+Xe are higher. The trend of decreasing power and specific impulse with increasing field in the Ar+Xe case is observed again here— the reasons for this are described in the previous paragraph. Regarding Xe only data, at 0.6T the specific impulse ranged from 1160 s at 250 V to 1470 s at 300 V, with corresponding powers of 1053 W and 1457 W respectively. At 0.8 T and 300 V, a lower power of 1162 W was measured. Fig. 6 b) has lines of efficiency overlaid on the data. At 0.8 T and 350 V, the specific impulse of 1560 s is a gain of 90 s with no loss of thrust per power (25 mN/kW) compared to 0.6 T and 300 V. At a fixed mass flow rate and discharge voltage, increasing the magnetic field leads to higher thrust per power, lower specific impulse and lower power utilisation. At fixed magnetic field and mass flow rate, increasing the voltage increased the specific impulse and reduced the thrust per power. Using an Ar+Xe gas mixture reduced the baseline performance, and caused it to be reduced further as the magnetic field increased due to discharge instabilities.

The error bars on the specific impulse measurements are large in all cases presented here, particularly in the cases with low mass flow rates. The cathode Mass Flow Controller (MFC) was operated at 1.8% of its maximum range, with error taken as 1.0% of its maximum range. By using a MFC with a specification closely matching the experiment requirements, these error bars could be reduced substantially. The thrust errorbars were reduced significantly over the course of the experiments by a) reducing wire friction, and b) switching off the cryocooler when taking measurements, and c) increasing the calibration force range. The thrust error could be further reduced by quantifying the magnetic interaction between the magnet, the vacuum chamber, and the thruster discharge current. The error in the power measurements was not considered significant. While many of these issues are common to all thruster performance measurements, some of them are specific to the challenges associated with integrating a HTS magnet with a thruster and thus identifying and finding methods to mitigate these issues are significant outcomes of this study.

Based on these results, we concluded that discharge voltages greater than 300 V would be necessary and that it was therefore critical to insulate electrical connections inside the vacuum chamber, in spite of this reducing the ease of thrust measurements. The convex anode configuration enabled higher field ignition. Xenon was superior to a mixture of Argon and Xenon because of increased performance, improved ignitability and better stability during discharge. We have also demonstrated the first conduction cooled HTS applied field magnet for an electric thruster.

4. Conclusions and further work

We have successfully demonstrated that a high temperature superconductor magnet can be used as an applied field module for a plasma thruster, with conduction cooling of the superconductor magnet. While the thruster was firing, the magnet and cryocooler system was used to produce a central field of 0.8 T with a power utilisation of $P_m + P_{cc} = 112$ W. A key finding of these experiments is that the cryogenic magnet and cryocooler system were able to function effectively for long durations near the hot thruster without exceeding critical temperature. The most extreme operating conditions demonstrated were operation with the magnet on, cryocooler off and the thruster firing. The integration of the magnet with the thruster and thrust stand involved many challenges, including abnormal discharges which damaged equipment, friction between wires preventing repeatable thrust stand response, and cryocooler vibration creating noise in thrust measurements. Solving these issues reduced risk to hardware, prevented different measurement systems from interfering with each other, and was a critical step in developing a system operation procedure which enabled precise and accurate thrust measurements to be collected during operation. The thruster was operated at a wide range of conditions, and through this sparse search we found a set of operating conditions that would allow reliable thruster ignition at high magnetic fields. The recommended practice is to use Xenon as the only ignition gas; use mass flow
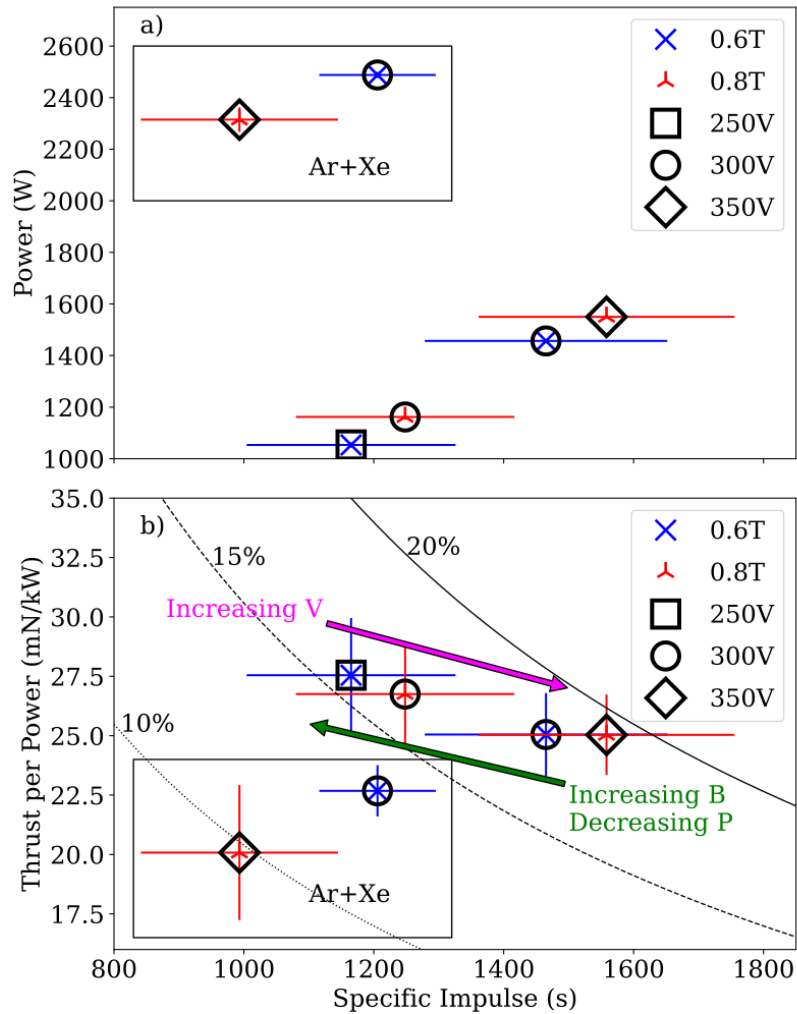
Figure 6: Thruster performance for the convex anode configuration, which enabled reliable thruster ignition at magnetic fields of up 0.8 T. a) shows power against specific impulse, and b) shows thrust per power against specific impulse, with electrical efficiency curves plotted in addition to test data. The power reported here is inclusive of the cathode keeper power, magnet power and cryocooler system power. The specific impulse is inclusive of cathode and anode mass flow rates. Propellant gas is Xe unless labelled otherwise.

rates greater than 2mg/s at the anode; adopt a convex anode configuration; and insulate electrical connections from anode discharge via the plasma (thus allowing higher anode discharge voltages to be utilised). In the convex anode configuration, specific impulse was found to increase with voltage, and decrease with magnetic field. Increasing the magnetic field enabled higher efficiencies to be achieved. Limits on low-power operation increased with increasing magnetic field, but efficiency increased with increasing field at the minimum discharge conditions. In this paper, we characterised the system and found reliable high-field operating conditions. These findings will enable future studies to perform systematic investigations on the role of the applied magnetic field in influencing the performance of the thruster at a grid of operating points.

5. Acknowledgments

References

[1] Dan M. Goebel and Ira Katz. *Fundamentals of Electric Propulsion: Ion and Hall Thrusters*. Wiley, 2008.

[2] John Brophy. The Dawn Ion Propulsion System. In *The Dawn Mission to Minor Planets 4 Vesta and 1 Ceres*, pages 251–261. Springer, 2012.

[3] Masatoshi Hirabayashi and Yuichi Tsuda. In *Hayabusa2 Asteroid Sample Return Mission: Technological Innovation and Advances*. Elsevier, 2022.

[4] Jacob Simmonds, Yevgeny Raitses, and Andrei Smolyakov. A theoretical thrust density limit for Hall thrusters. *Journal of Electric Propulsion*, 2(1):Art. 12, March 2023.

[5] Mark Crofton, J. Pollard, E. Beiting, R. Spektor, K. Diamant, X. Eapen, R. Cohen, and Michael Patterson. Characterization of the NASA NEXT Thruster. In *45th AIAA/ASME/SAE/ASEE Joint Propulsion Conference & Exhibit*, page Art. 4815. American Institute of Aeronautics and Astronautics, August 2009.

[6] K. Diamant, T. Curtiss, R. Spektor, E. Beiting, V. Hruby, B. Pote, J. Kolencik, and S. Paintal. Performance and Plume Characterization of the BHT-1500 Hall Thruster. In *Proceedings of the 34th International Electric Propulsion Conference*, Hyogo-Kobe, Japan, 2015. IEPC.

[7] R. L. Burton, K. E. Clark, and R. G. Jahn. Measured performance of a multimegawatt MPD thruster. *Journal of Spacecraft and Rockets*, 20(3):299–304, May 1983.

[8] Marcus Collier-Wright, Elias Boegel, Manuel La Rosa Betancourt, Georg Herdrich, Alexander Behnke, Bartomeu Massuti Ballester, and Veit Grosse. High-temperature superconductor-based power and propulsion system architectures as enablers for high power missions. *Acta Astronautica*, 201:198–208, December 2022.

[9] A Sasoh, K Mizutani, and A Iwakawa. Electrostatic/magnetic ion acceleration through a slowly diverging magnetic nozzle between a ring anode and an on-axis hollow cathode. *AIP Advances*, 7(6), June 2017.

[10] D. Ichihara, R. Nakano, Y. Nakamura, K. Kinefuchi, and A. Sasoh. Electrostatic-magnetic hybrid ion acceleration for high-thrust-density operation. *Journal of Applied Physics*, 130(22), December 2021.

[11] Jakob Balkenhohl, Jakub Glowacki, Nicholas Rattenbury, and John Cater. A review of low-power applied-field magnetoplasmadynamic thruster research and the development of an improved performance model. *Journal of Electric Propulsion*, 2(1):Art. 1, January 2023.

[12] Dan R. Lev and Edgar Y. Choueiri. Scaling of Efficiency with Applied Magnetic Field in Magnetoplasmadynamic Thrusters. *Journal of Propulsion and Power*, 28(3):609–616, May 2012.

[13] Akihiro Sasoh, Hayato Kasuga, Yoshiya Nakagawa, Toshihiro Matsuba, Daisuke Ichihara, and Akira Iwakawa. Electrostatic-magnetic-hybrid thrust generation in central-cathode electrostatic thruster (cc-est). *Acta Astronautica*, 152:137–145, November 2018.

[14] Daisuke Ichihara, Tomoki Uno, Hisashi Kataoka, Jaehun Jeong, Akira Iwakawa, and Akihiro Sasoh. Ten-Ampere-Level, Applied-Field-Dominant Operation in Magnetoplasmadynamic Thrusters. *Journal of Propulsion and Power*, 33(2):360–369, March 2017.

[15] A. S. Voronov, A. A. Troitskiy, I. D. Egorov, S. V. Samoilenkov, and A. P. Vavilov. Magnetoplasmadynamic thruster with an applied field based on the second generation high-temperature superconductors. *Journal of Physics: Conference Series*, 1686(1):Art. 012023, December 2020.

[16] Hirokazu Tahara, Yoichi Kagaya, and Takao Yoshikawa. Ten-Ampere-Level, Applied-Field-Dominant Operation in Magnetoplasmadynamic Thrusters. *Journal of Propulsion and Power*, 13(5):651–658, September 1997.

[17] Jinxing Zheng, Haiyang Liu, Yuntao Song, Cheng Zhou, Yong Li, Ming Li, Haibin Tang, Ge Wang, Yuntian Cong, Baojun Wang, Yibai Wang, Peng Wu, Timing Qu, Xiaoliang Zhu, Lei Zhu, Fei Liu, Yuan Cheng, and Boqiang Zhao. Integrated study on the comprehensive magnetic-field configuration performance in the 150 kW superconducting magnetoplasmadynamic thruster. *Scientific Reports*, 11(1):Art. 20706, October 2021.

[18] Jakub Glowacki, Rodney A. Badcock, and Nicholas Long. Design analysis of a plasma thruster with superconducting magnets. *AIAA Propulsion and Energy 2019 Forum*, Art. 4081, August 2019.

[19] Chris Acheson, Jakub Glowacki, Tulasi Parashar, and Stuart C. Wimbush. Computational Modelling of AF-MPDTs: How does Magnetic Shielding Influence Thrust? In *Proceedings of the 37th International Electric Propulsion Conference*, Massachusetts Institute of Technology, USA, June 2022. IEPC.

[20] H. W. Weijers, U. P. Trociewitz, W. D. Markiewicz, J. Jiang, D. Myers, E. E. Hellstrom, A. Xu, J. Jaroszynski, P. Noyes, Y. Viouchkov, and D. C. Larbalestier. High Field Magnets With HTS Conductors. *IEEE Transactions on Applied Superconductivity*, 20(3):576–582, June 2010.

[21] Valerio Calvelli, Riccardo Musenich, Filippo Tunesi, and Roberto Battiston. A Novel Configuration for Superconducting Space Radiation Shields. *IEEE Transactions on Applied Superconductivity*, 27(4):1–4, June 2017.

[22] K. Matsuo, Y. Miyazato, and H.-D. Kim. Hybrid power sources (HPSs) for space applications: Analysis of PEMFC/Battery/SMES HPS under unknown load containing pulses. *Renewable and Sustainable Energy Reviews*, 105:14–37, 2019.

[23] Jamal R. Olatunji, Nicholas M. Strickland, Max R. Goddard Winchester, Kiyoshi Kinefuchi, Daisuke Ichihara, Nicholas J. Long, and Stuart C. Wimbush. Modelling of a 1 T High-Temperature Superconducting Applied Field Module for a Magnetoplasmadynamic Thruster. *TENCON 2021 - 2021 IEEE Region 10 Conference (TENCON)*, pages 173–178, December 2021.

[24] R. Nakano, D. Ichihara, K. Takahara, and A. Sasoh. Improvement of near anode ionization effect on electrostatic-magnetic hybrid ion acceleration by anode shape and magnetic distribution. *JSASS*, Art. 4592, 2022.

[25] Xing Han, Zun Zhang, Zhiyuan Chen, Marco Marano, Haibin Tang, and Jinbin Cao. High-spatial-resolution image reconstruction-based method for measuring electron temperature and density of the very near field of an applied-field magnetoplasmadynamic thruster. *Journal of Physics D: Applied Physics*, 54(13):Art. 135203, January 2021.

[26] Z. Y. Chen, Y. B. Wang, J. X. Ren, P. Wu, M. Li, and H. B. Tang. Numerical investigation of "Detachment cone" in the magnetic nozzle. In *Proceedings of the 36th International Electric Propulsion Conference*, Vienna, Austria, September 2019. IEPC.

[27] Seungyong Hahn, Dong Keun Park, Juan Bascunan, and Yukikazu Iwasa. HTS Pancake Coils Without Turn-to-Turn Insulation. *IEEE Transactions on Applied Superconductivity*, 21(3):1592–1595, June 2011.

[28] J. R. Olatunji, H. W. Weijers, N. M. Strickland, and S. C. Wimbush. Modelling the Quench Behavior of an NI HTS Applied-Field Module for a Magnetoplasmadynamic Thruster Undergoing a 1kW Discharge. *IEEE Transactions on Applied Superconductivity*, 33(5):1–6, August 2023.

[29] Eduardo Ahedo and Mario Merino. On plasma detachment in propulsive magnetic nozzles. *Physics of Plasmas*, 18(5), May 2011.